

Assessing quantum coherence in quantum annealers

Connor Aronoff,¹ Travis Howard,¹ David Nicholaeff,² Alejandro Lopez-Bezanilla,³ and Wade DeGottardi¹

¹*Department of Physics and Astronomy, Texas Tech University,
Texas Tech University, Lubbock, TX 79409-1051, USA**

²*New Mexico Consortium, Los Alamos, New Mexico 87544, USA*

³*Theoretical Division, Los Alamos National Laboratory, Los Alamos, New Mexico 87545, USA*

(Dated: February 26, 2026)

Demonstrating genuine many-body quantum coherence in large-scale quantum processors remains a central challenge for near-term quantum technologies. Recent experiments on D-Wave quantum annealers have investigated quenches of Ising chains and observed defect densities that show Kibble–Zurek scaling, consistent with coherent quantum dynamics. However, identical scaling can arise from classical or thermal processes. Here we propose the use of many-body coherent oscillations (MBCO) as a diagnostic for the identification of system-wide coherence in analog quantum simulators. Solving the time-dependent Schrödinger equation, we show that quenches of a staggered one-dimensional Ising chain across a quantum critical point produce oscillatory signatures in defect observables. We implement this model on the D-Wave Advantage quantum annealer. Using fast-anneal protocols, we find that, although defect densities follow Kibble–Zurek scaling, the expected oscillatory behavior is absent. We demonstrate that static disorder associated with individual qubits is not likely responsible for the absence of MBCO. Modest modifications to annealing schedules can dramatically enhance oscillation visibility. This work gives a general roadmap for the search for quantum coherence in noisy, large-scale quantum platforms.

The design of quantum information processors needs to reconcile the competing demands of coherence and scalability. While long coherence times can be achieved in small systems of well-isolated qubits, maintaining coherent dynamics in large, highly connected architectures remains a principal obstacle to scalable quantum computation [1–3]. Recent technological advances have enabled the fabrication of superconducting circuits containing thousands of controllable qubits, establishing a powerful platform for exploring collective quantum dynamics at scale. Among these architectures, quantum annealers occupy a distinctive niche: rather than implementing gate sequences, they exploit time-dependent Hamiltonian evolution and quantum tunneling to search for low-energy configurations of optimization problems [4–7]. Achieving large connectivity and precise control in such systems, however, comes at the cost of increased exposure to decoherence arising from macroscopic circuitry, control lines, and flux noise [1, 8–14].

Assessing whether these devices sustain genuine many-body quantum coherence is therefore both essential and challenging. Recently, research on the D-Wave Advantage quantum annealer, a machine with 4500 superconducting flux qubits, reported observations of coherent dynamics in a programmed one-dimensional transverse-field Ising chain [15–17]. These experiments involve quenching the system from a paramagnetic to a ferromagnetic phase, producing domain-wall defects whose density scales with anneal time in accordance with predictions of the Kibble–Zurek mechanism (KZM) [18–22]. While such scaling is consistent with quantum critical dynamics, the same power law can arise from classical

processes. In fact, the diffusion–annihilation of domain walls in one dimension yields an identical power-law exponent [23, 24], although a detailed statistical analysis presented in Ref. [15] suggests that these processes alone cannot fully account for the results. Scaling behavior alone constitutes circumstantial rather than definitive evidence of quantum coherence.

This ambiguity highlights a broader conceptual gap: what observables provide clear evidence of coherent many-body quantum dynamics in noisy, large-scale quantum simulators? Oscillatory behavior, whether in space or time, is a hallmark of quantum coherence. Spatial Friedel oscillations reflect the coherence of fermionic quasiparticles near a Fermi surface [25], while temporal Stückelberg oscillations arise when a system is driven through multiple quantum critical points, resulting in interference between distinct excitation pathways. The latter have been theoretically predicted in one-dimensional Ising chains [26, 27] where they manifest as oscillations in defect observables following a quench. The observation of these many-body coherent oscillations (MBCO) would provide a clear signature of quantumness.

In this work, we propose MBCO as a phase-sensitive diagnostic of quantum coherence in analog quantum annealers. We first articulate three criteria necessary for MBCO to exist and be observable on a quantum annealer. Focusing on a staggered one-dimensional Ising chain [26, 28–30], we show theoretically that quenches across a quantum critical point generate oscillatory signatures in defect observables arising from many-body quantum interference, which are robust to static disorder. We implement this model on a quantum annealer and perform a systematic search for MBCO using fast-anneal protocols. While the measured defect densities reproduce Kibble–Zurek scaling, the absence of oscilla-

* coaronof@ttu.edu

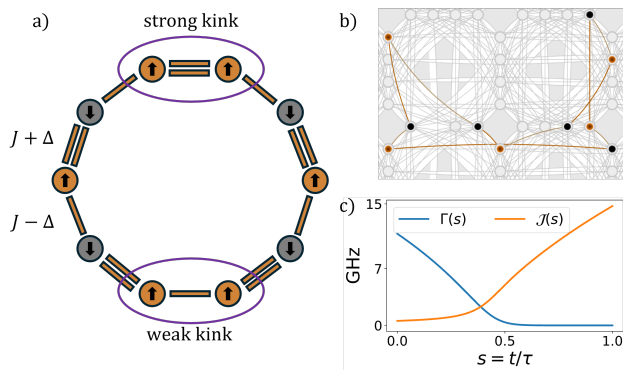


FIG. 1. (a) The staggered Ising chain with alternating strong ($J + \Delta$) and weak ($J - \Delta$) bond strengths. For an antiferromagnetic chain, kinks correspond to neighboring spins that are parallel after a quench. (b) Embedding of a staggered 10-qubit Ising chain on the D-Wave Advantage machine. The coloring of the qubits indicate the results of an anneal, with spin-up and spin-down indicated by orange and gray, respectively. (c) D-Wave annealing schedule [31] for the couplings $\mathcal{J}(s)$ and $\Gamma(s)$ in Hamiltonian (1) as a function of the anneal parameter $s = t/\tau$.

tory signatures places quantitative bounds on coherent many-body dynamics under current operating conditions and highlights the need for interference-based analysis beyond scaling laws to certify quantumness in large-scale quantum devices.

Before describing our search for MBCO, we identify several key prerequisites for their detection. (1) The annealing time τ must not exceed the qubit coherence time, which is 5–50 nsec for D-Wave [31]. (2) The detection of oscillations of frequency Ω requires data with a sampling precision $\Delta\tau$ that satisfies the Nyquist-Shannon condition $\Omega < 1/2\Delta\tau$ [32, 33]. (3) The energy of the MBCO must exceed $k_B T$. A temperature $T^* \lesssim \hbar\Omega/k_B$, where k_B and h are the Boltzmann and Planck constants, allows for the detection of a single quanta in principle. Conditions (1)-(3) are satisfied using D-Wave’s fast-anneal protocol. Condition (1) is satisfied given anneals as short as $\tau \approx 5$ nsec are accessible. The MBCO considered here have a frequency $\Omega \approx 5$ GHz. For annealing times $\tau \sim 10$ nsec, the precision $\Delta\tau \sim 20$ psec, which, according to the Nyquist-Shannon condition (2), allows the detection of oscillations $\Omega \lesssim 25$ GHz. Condition (3) gives a maximum temperature of $T^* \approx 250$ mK for $\Omega \approx 5$ GHz, while D-Wave operates at 12-15 mK.

The time-dependent Hamiltonian of the staggered Ising chain [29, 30] is

$$H(s)/h = \mathcal{J}(s) \sum_{n=0}^N (J + \Delta(-1)^n) \sigma_n^z \sigma_{n+1}^z + \Gamma(s) \sum_n \sigma_n^x, \quad (1)$$

where the annealing parameter $s = t/\tau$, t is time, τ is the duration of the anneal, and σ_n^x and σ_n^z denote the Pauli spin operators for the n^{th} qubit. The time-dependent frequencies $\mathcal{J}(s) \geq 0$ and $\Gamma(s) \geq 0$ set the relative strength

of the ferromagnetic and paramagnetic terms, while the dimensionless parameters $J, \Delta > 0$ set the staggering strength. As shown in Figure 1a, the Hamiltonian (1) is characterized by alternating strong and weak couplings proportional to $J + \Delta$ and $J - \Delta$, respectively.

Figure 1b shows the D-Wave annealing schedules for the transverse field $\Gamma(s)$ and the Ising coupling $\mathcal{J}(s)$. At the start of the anneal, $\mathcal{J}(0) = 0$ and $\Gamma(0) \approx 11$ GHz, deep in the paramagnetic phase. At the end of the anneal the system is in the ferromagnetic phase with $\mathcal{J}(1) \approx 15$ GHz and $\Gamma(1) = 0$. The boundary between these two phases is given by

$$\sqrt{J^2 + \Delta^2} \mathcal{J}(s) = \Gamma(s) \quad (2)$$

[26, 34]. Near the critical point, quantum fluctuations give rise to topological defects, i.e., domain-wall kinks. For the antiferromagnetic chain, these defects are associated with coupled spins that are parallel after the anneal, see Figure 1a. The expectation value of the total defect density, which is the number of defects per qubit, is $K(\tau) = \frac{1}{2N} \sum_n (1 + \langle \sigma_n^z \sigma_{n+1}^z \rangle_{s=1})$ at the end of the anneal ($s = 1$). The difference in the kink densities across weak and strong bonds is

$$P(\tau) = \frac{1}{2N} \sum_n (-1)^n \langle \sigma_n^z \sigma_{n+1}^z \rangle_{s=1}. \quad (3)$$

The quantity $P > 0$ since fewer defects are expected across strong bonds ($J + \Delta$) than weak bonds ($J - \Delta$).

The staggered Ising chain can be solved exactly via a Jordan-Wigner transformation in which spinless fermions $\psi_n = \frac{1}{2} \prod_{j=1}^{n-1} \sigma_j^x (\sigma_n^z + i\sigma_n^y)$ are introduced at each site n [26, 28, 34]. The resultant fermionic Hamiltonian is quadratic (see the Supplementary Material). In k -space, the Hamiltonian is block-diagonal. For the initial conditions considered here, these blocks can be taken to be 6×6 matrices. Calculating the number of defects is thus reduced to solving the time-dependent Schrödinger equation for each of these blocks. For sufficiently long quenches, the total number of kinks follows Kibble-Zurek scaling [21]. The theoretical prediction for the difference in kink densities $P(\tau)$ across strong and weak bonds for particular values of J and Δ is shown in Figure 2b for short annealing times. The number of defects is found to oscillate, with some beating, at a frequency $\Omega \sim \mathcal{J}(s_c)\Delta$, where $s_c \approx 1/3$ is the annealing parameter at criticality. The Fourier transform of $P(\tau)$, shown in Figure 2c, reveals a sharp feature at $\Omega \approx 5.4$ GHz. The sensitivity of $S(\Omega)$ to the range of annealing times is discussed in the Supplementary Material.

We conducted a systematic search for MBCO on the D-Wave Advantage system. Our quantum simulations implemented fast quenches of multiple realizations of the staggered Ising chain embedded as rings of 160 qubits, as shown in Figure 6. Before acquiring data on D-Wave, we carried out a calibration procedure known as shimming to account for variations associated with individual qubit biases and coupler strengths. For details, refer to

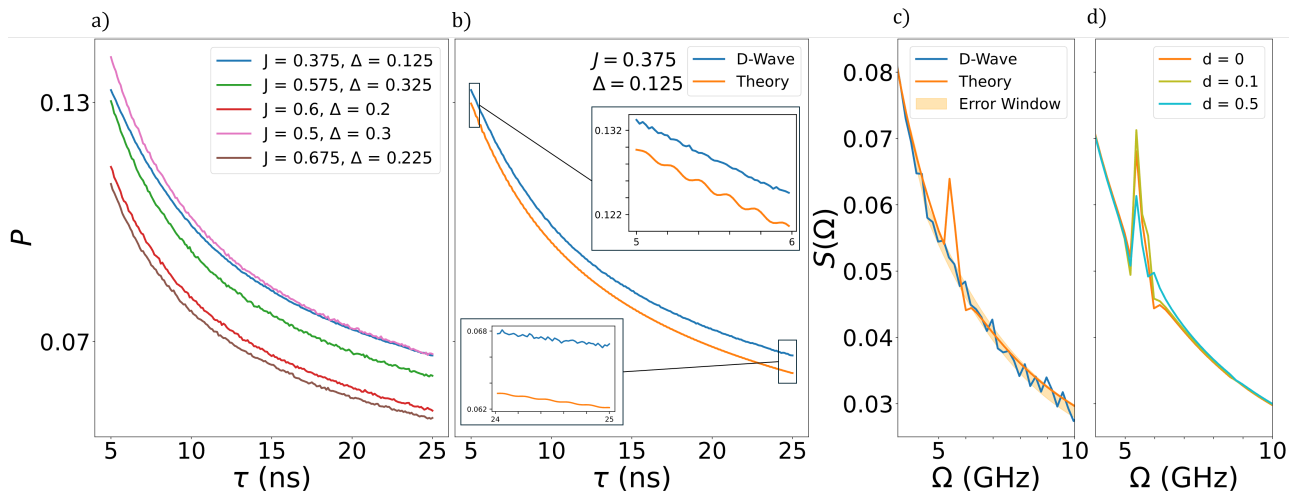


FIG. 2. (a) The average difference in kink densities across weak and strong bonds P for annealing times in the reported coherent regime $5 \text{ ns} \leq \tau \leq 25 \text{ ns}$ for staggered Ising chains of length $L = 160$ obtained from D-Wave fast-quench anneals. Each line represents the mean of approximately 75,000 anneals for the indicated bond strengths J and Δ . (b) P for D-Wave (blue) and theory (orange) for $J = 0.375$ and $\Delta = 0.125$. Magnified insets show theoretically predicted many-body coherent oscillations are most pronounced for annealing times $\tau \lesssim 15 \text{ ns}$. These oscillations are absent in the D-Wave data. (c) Fourier transform $S(\Omega)$ of $P(\tau)$ for D-Wave data and theory from (b). Theoretical curve for $S(\Omega)$ exhibits a well-defined peak at $\Omega \approx 5.4 \text{ GHz}$. The error window (orange band) has a full width corresponding to 2σ . (d) Fourier transform $S(\Omega)$ for the theoretical model accounting for disorder in Zeeman field, where d is the strength of the disorder. We find that the prominent feature at $\Omega \approx 5.4 \text{ GHz}$ is robust to strong disorder.

Figure 5 of Supplementary Material. In total, 90,000 fast anneals processes were conducted for each annealing time τ . The first 15,000 anneals were used for the shimming process and 75,000 anneals contributed to the usable data.

The curves in Figure 2a show $P(\tau)$ obtained from these 75,000 anneals for 200 different annealing times τ . A discrete Fourier transform of the data shown in Figure 2b yields the jagged blue curve in Figure 2c. To quantify the statistical uncertainty in the Fourier amplitudes $S(\Omega)$, the data was partitioned into 75,000 artificial time series by random assignment. Each series was Fourier transformed, and the standard deviation of the spectra defined the frequency-resolved noise level $\sigma(\Omega)$. The shaded band in Figure 2c indicates the 2σ window about the best-fit noise baseline. Repeating the randomization procedure with different time series produced indistinguishable noise estimates, confirming the robustness of the extracted $\sigma(\Omega)$.

Despite the fact that our search was conducted in D-Wave's putative coherent regime, the collected data shows no evidence of the predicted oscillations, although the measured defect densities are consistent with the predictions of Kibble-Zurek (KZ) theory (see Supplementary Material). The spectrum $S(\Omega)$, obtained by Fourier transforming the analytical-derived curve in Figure 2b, exhibits a peak near $\Omega \approx 5.4 \text{ GHz}$ and is more than 5σ above the center of the noise window (yellow band). The Fourier transform of the D-Wave data shows no discernible structure at this frequency. This allows us to state with high confidence that the predicted oscillations

are absent in the annealer-derived data.

A potential source of the discrepancy between theory and experiment is the static disorder in the quantum annealer, which could suppress coherent oscillations. Such disorder can arise from variations in the flux qubits and their couplings to control lines. Disorder of this type can be partially mitigated through shimming, a calibration procedure that reduces the spread in the effective programmed couplings $\mathcal{J}(s)J_n$ and anneal offsets (see Supplementary Material), where J_n is the effective coupling strength for the n^{th} qubit. However, there is no way to address any potential disorder in the Zeeman-like terms σ_n^x . To investigate its impact, we consider a generalization of our Hamiltonian in which Zeeman-like terms in Eq. (1) are replaced by $\Gamma(s) \sum_n h_n \sigma_n^x$, with $h_n = 1 + dx_n$ and x_n is drawn uniformly from $[-1, 1]$. The disorder gives rise to terms in the Hamiltonian of the form $h_{2k} \psi_k^\dagger \psi_{-k}$ in the corresponding fermionic theory, where ψ_k is the annihilation operator of a fermion with wave number k and h_{2k} is the Fourier transform of h_n . These terms describe backscattering of the fermionic quasiparticles of the system. Remarkably, as shown in Figure 2, the many-body coherent oscillations remain robust over a wide range of disorder strengths d , and persist even as the disorder d approaches 0.5. This result, together with our detailed shimming procedure, rules out static disorder as a likely cause for the absence of coherent oscillations in the D-Wave data.

Although our theory predicts that the MBCO should in principle be observable on the D-Wave platform, their visibility is small (see Figure 2b). We therefore propose

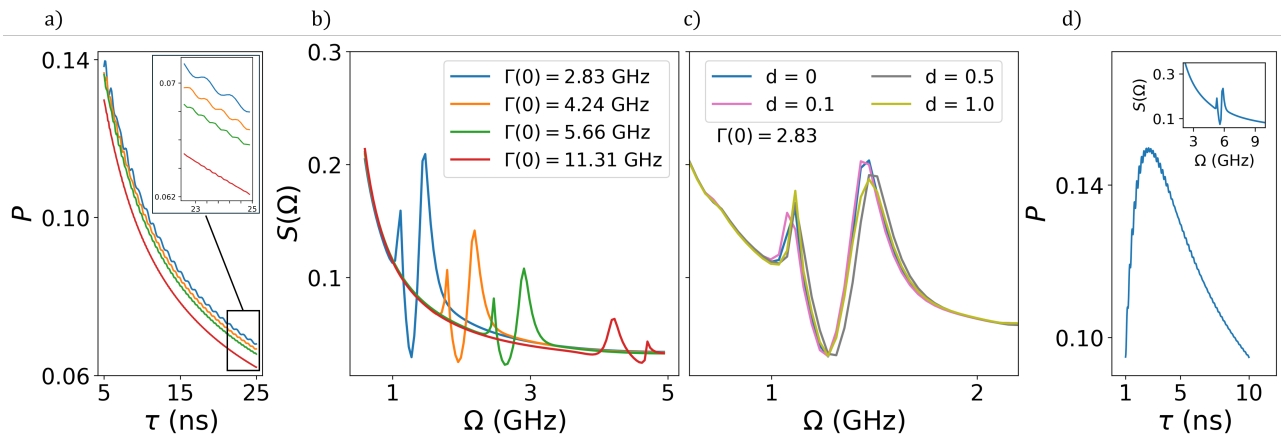


FIG. 3. Theoretical results for annealing parameters beyond the range currently accessible on D-Wave. (a) Calculated expectation value of the difference in kink densities P as a function of annealing time τ for various initial strengths of the parameter $\Gamma(0)$ (see legend in (b)). For these values of $\Gamma(0)$, a doublet peak structure in $S(\Omega)$ is visible. (b) Peaks in the Fourier transform of $S(\Omega)$ of P become more prominent as $\Gamma(0)$ is decreased, in agreement with (a). (c) $S(\Omega)$ for $\Gamma(0) = 2.83$ GHz and various disorder strengths d . (d) $P(\tau)$ for ultra-short anneal times ($\tau < 5$ ns). (Inset) Fourier transform $S(\Omega)$ of $P(\tau)$.

modifications of the annealing schedule that substantially enhance the visibility of the MBCO. One way to accomplish this is to reduce the scale of the transverse field $\Gamma(s)$ from its current value $\Gamma(0) \approx 11$ GHz. Theoretical curves for $P(\tau)$ for several values of $\Gamma(0)$ are shown in Figure 3a. A second modification involves shortening the annealing time τ . As shown in Figure 3b, reducing it to $\tau \approx 2.5$ ns leads to increased visibilities. Stückelberg oscillations are typically associated with quenches in which several quantum critical points are crossed. A likely reason for the small oscillations here is that only one quantum critical point is crossed during the anneal. In so-called “reverse anneals,” it may be possible to cross more than one critical point, however fast reverse anneals are not currently available to D-Wave users.

We have shown that a staggered one-dimensional Ising chain provides an analytically controlled and experimentally accessible diagnostic for probing many-body quantum coherence in large-scale quantum simulators. The quench dynamics of this system generate many-body coherent oscillations arising from quantum interference and offer a sophisticated test for many-body quantum coherence. While the rigorous requirements for observing these oscillations—fast control, high temporal resolution, and sustained phase coherence—are, in principle, met by recently introduced fast-anneal capabilities, our searches reveal no evidence of the predicted oscillatory signatures on the staggered Ising chain. Furthermore, our analysis rules out static disorder as a likely culprit. These findings underscore a central challenge for quantum annealing architectures: achieving precise, system-wide synchronization across thousands of qubits during time-dependent evolution. For example, even small mismatches in tim-

ing or control amplitudes can induce collective dephasing, suppressing the many-body interference effects that distinguish genuine quantum dynamics from classical or incoherent behavior.

Beyond diagnosing current limitations, our results establish a clear roadmap for future progress. We demonstrate that modest modifications to annealing schedules can dramatically enhance the visibility of many-body coherent oscillations, suggesting concrete directions for hardware and control improvements. Specifically, our results point to greater schedule flexibility and reduced transverse-field scales as a way of accessing coherent many-body interference in quantum annealers. More broadly, this work highlights that power-law defect scaling alone is insufficient to certify quantumness in noisy, large-scale quantum systems. Instead, interference-based observables such as MBCO provide a sharp signature of many-body coherence. Targeted searches for these oscillations therefore offer a powerful and broadly applicable framework for validating quantum coherence in next-generation analog quantum simulators.

Los Alamos National Laboratory is managed by Triad National Security, LLC, for the National Nuclear Security Administration of the U.S. Department of Energy under Contract No. 89233218CNA000001. The authors thank the New Mexico Consortium, under subcontract C2778, the Quantum Cloud Access Project (QCAP), for providing quantum computing resources and technical collaboration. We gratefully acknowledge discussions with Gabe Schumm, Anders W. Sandvik, and Chris Rich. We are especially grateful to Andrew King for numerous enlightening discussions.

-
- [1] Wendin, G. Quantum information processing with superconducting circuits: a review. *Reports on Progress in Physics* **80**, 106001 (2017).
- [2] Gill, S. S. *et al.* Quantum computing: A taxonomy, systematic review and future directions. *Software: Practice and Experience* **52**, 66–114 (2022).
- [3] de Leon, N. P. *et al.* Materials challenges and opportunities for quantum computing hardware. *Science* **372**, eabb2823 (2021).
- [4] Apolloni, B., Carvalho, C. & De Falco, D. Quantum stochastic optimization. *Stochastic Processes and their Applications* **33**, 233–244 (1989).
- [5] Finnila, A. B., Gomez, M. A., Sebenik, C., Stenson, C. & Doll, J. D. Quantum Annealing: A New Method for Minimizing Multidimensional Functions. *Chemical Physics Letters* **219**, 343–348 (1994).
- [6] Kadowaki, T. & Nishimori, H. Quantum annealing in the transverse Ising model. *Physical Review E* **58**, 5355–5363 (1998).
- [7] Johnson, M. W. *et al.* Quantum annealing with manufactured spins. *Nature* **473**, 194–198 (2011).
- [8] Clarke, J. & Wilhelm, F. K. Superconducting quantum bits. *Nature* **453**, 1031–1042 (2008).
- [9] Bunyk, P. I. *et al.* Architectural Considerations in the Design of a Superconducting Quantum Annealing Processor. *IEEE Transactions on Applied Superconductivity* **24**, 1–10 (2014).
- [10] Chancellor, N., Zohren, S. & Warburton, P. A. Circuit design for multi-body interactions in superconducting quantum annealing systems with applications to a scalable architecture. *npj Quantum Information* **3**, 21 (2017).
- [11] Das, S. & Agarwal, G. S. Decoherence effects in interacting qubits under the influence of various environments. *Journal of Physics B: Atomic, Molecular and Optical Physics* **42**, 229801 (2009).
- [12] Nguyen, L. B. *et al.* High-Coherence Fluxonium Qubit. *Physical Review X* **9**, 041041 (2019).
- [13] Tuokkola, M. *et al.* Methods to achieve near-millisecond energy relaxation and dephasing times for a superconducting transmon qubit. *Nature Communications* **16**, 5421 (2025).
- [14] Ganjam, S. *et al.* Surpassing millisecond coherence in on chip superconducting quantum memories by optimizing materials and circuit design. *Nature Communications* **15**, 3687 (2024).
- [15] King, A. D. *et al.* Coherent quantum annealing in a programmable 2,000 qubit Ising chain. *Nature Physics* **18**, 1324–1328 (2022).
- [16] King, A. D. *et al.* Computational supremacy in quantum simulation (2024). ArXiv:2403.00910 [quant-ph].
- [17] Bando, Y. *et al.* Probing the universality of topological defect formation in a quantum annealer: Kibble-Zurek mechanism and beyond. *Physical Review Research* **2**, 033369 (2020).
- [18] Kibble, T. W. B. Topology of cosmic domains and strings. *Journal of Physics A: Mathematical and General* **9**, 1387 (1976).
- [19] Zurek, W. H. Cosmological experiments in superfluid helium? *Nature* **317**, 505–508 (1985).
- [20] Campo, A. d. & Zurek, W. H. Universality of Phase Transition Dynamics: Topological Defects from Symmetry Breaking. *International Journal of Modern Physics A* **29**, 1430018 (2014).
- [21] Huang, Y., Yin, S., Feng, B. & Zhong, F. Kibble-Zurek mechanism and finite-time scaling. *Physical Review B* **90**, 134108 (2014).
- [22] Chandran, A., Erez, A., Gubser, S. S. & Sondhi, S. L. Kibble-Zurek problem: Universality and the scaling limit. *Physical Review B* **86**, 064304 (2012).
- [23] Zwerger, W. Critical slowing down of diffusion in a one-dimensional kinetic Ising model. *Physics Letters A* **84**, 269–270 (1981).
- [24] Krebs, K., Pfannmüller, M. P., Wehefritz, B. & Hinrichsen, H. Finite-size scaling studies of one-dimensional reaction-diffusion systems. Part I. Analytical results. *Journal of Statistical Physics* **78**, 1429–1470 (1995).
- [25] Simion, G. E. & Giuliani, G. F. Friedel oscillations in a Fermi liquid. *Physical Review B* **72**, 045127 (2005).
- [26] Yan, B., Chernyak, V. Y., Zurek, W. H. & Sinitsyn, N. A. Nonadiabatic Phase Transition with Broken Chiral Symmetry. *Physical Review Letters* **126**, 070602 (2021).
- [27] Bayocboc, F. A., Dziarmaga, J., Rams, M. M. & Zurek, W. H. Persistent oscillation of a Cooper-pair condensate of topological defects in a nonintegrable quantum Ising chain. *Physical Review B* **111**, L100406 (2025).
- [28] Iglói, F. & Zittartz, J. Quantum Ising model with staggered interaction. *Zeitschrift für Physik B Condensed Matter* **70**, 387–393 (1988).
- [29] Reichardt, B. W. The quantum adiabatic optimization algorithm and local minima. In *Proceedings of the thirty-sixth annual ACM symposium on Theory of computing, STOC '04*, 502–510 (Association for Computing Machinery, New York, NY, USA, 2004).
- [30] Mishra, A., Albash, T. & Lidar, D. A. Finite temperature quantum annealing solving exponentially small gap problem with non-monotonic success probability. *Nature Communications* **9**, 2917 (2018).
- [31] Annealing Implementation and Controls. URL https://docs.dwavequantum.com/en/latest/quantum_research/annealing.html.
- [32] Nyquist, H. Certain Topics in Telegraph Transmission Theory. *Transactions of the American Institute of Electrical Engineers* **47**, 617–644 (1928).
- [33] Shannon, C. Communication in the Presence of Noise. *Proceedings of the IRE* **37**, 10–21 (1949).
- [34] Zhang, D.-g., Li, B.-z. & Li, Y. The exact solution of the Ising quantum chain with alternating single and sector defects. *Physics Letters A* **186**, 47–50 (1994).
- [35] Chern, K., Boothby, K., Raymond, J., Farré, P. & King, A. D. Tutorial: Calibration refinement in quantum annealing. *Frontiers in Computer Science* **5**, 1238988 (2023).
- [36] VirtualGraphComposite — dwave-system 0.3.2 documentation. URL https://dwave-systemdocs.readthedocs.io/en/link_fix/reference/composites/virtual_graph.html.
- [37] Errors and Error Correction. URL https://docs.dwavequantum.com/en/latest/quantum_research/errors.html.

I. SUPPLEMENTAL MATERIAL

A. Exact Solution for the Staggered Ising Chain

The Hamiltonian of the staggered Ising chain is

$$H = \sum_n (J + \Delta(-1)^n) \sigma_n^z \sigma_{n+1}^z + h \sum_n \sigma_n^x. \quad (4)$$

We apply a Jordan-Wigner transformation

$$\psi_n = \frac{1}{2} \prod_{j=1}^{n-1} \sigma_j^x (\sigma_n^z + i\sigma_n^y). \quad (5)$$

The fermion operators obey anti-commutation relations $\{\psi_n^\dagger, \psi_{n'}\} = \delta_{nn'}$. In terms of the fermions, the Hamiltonian (4) is

$$H = \sum_n [J + \Delta(-1)^n] (\psi_n \psi_{n+1} - \psi_n^\dagger \psi_{n+1}^\dagger - \psi_n^\dagger \psi_{n+1} - \psi_{n+1}^\dagger \psi_n) + h(2\psi_n^\dagger \psi_n - 1). \quad (6)$$

Going to k -space, we have $\psi_n = \frac{1}{\sqrt{N}} \sum_k e^{ikn} \psi_k$, which gives

$$\begin{aligned} H = & \sum_k J (e^{-ik} \psi_k \psi_{-k} + e^{-ik} \psi_k^\dagger \psi_{-k}^\dagger - e^{ik} \psi_k^\dagger \psi_k - e^{-ik} \psi_k^\dagger \psi_k) \\ & + \Delta (-e^{-ik} \psi_k \psi_{\pi-k} + e^{-ik} \psi_k^\dagger \psi_{\pi-k}^\dagger + e^{ik} \psi_k^\dagger \psi_{\pi+k} - e^{-ik} \psi_k^\dagger \psi_{\pi+k}) \\ & + h(2\psi_k^\dagger \psi_k - 1). \end{aligned}$$

The allowed values of $k = 2\pi j/N$, for $0 \leq j \leq N$. The Hamiltonian couples fermion modes with wave numbers k , $-k$, $\pi + k$, and $\pi - k$. We work in the basis $|n_k, n_{-k}, n_{\pi-k}, n_{\pi+k}\rangle$ where $n_k = \psi_k^\dagger \psi_k$. The initial state of the system is $|0, 0, 0, 0\rangle$. For this initial state, only six states are accessible: $|1, 1, 1, 1\rangle$, $|1, 1, 0, 0\rangle$, $|1, 0, 1, 0\rangle$, $|0, 1, 0, 1\rangle$, $|0, 0, 1, 1\rangle$ and $|0, 0, 0, 0\rangle$.

Thus, the Hamiltonian can be expressed in terms of 6×6 blocks,

$$H = \sum_{0 < k < \pi/2} \hat{\Psi}_k^\dagger H_k \hat{\Psi}_k, \quad (7)$$

where now the allowed values of k are restricted to the range indicated and

$$H_k = \begin{bmatrix} 4h & -2Ji \sin k & -2\Delta \cos k & -2\Delta \cos k & -2Ji \sin k & 0 \\ 2Ji \sin k & -4J \cos k & -2i\Delta \sin k & -2i\Delta \sin k & 0 & -2iJ \sin k \\ -2\Delta \cos k & 2i\Delta \sin k & 0 & 0 & -2i\Delta \sin k & 2\Delta \cos k \\ -2\Delta \cos k & 2i\Delta \sin k & 0 & 0 & -2i\Delta \sin k & 2\Delta \cos k \\ 2Ji \sin k & 0 & 2i\Delta \sin k & 2i\Delta \sin k & 4J \cos k & -2iJ \sin k \\ 0 & 2iJ \sin k & 2\Delta \cos k & 2\Delta \cos k & 2iJ \sin k & -4h \end{bmatrix},$$

and

$$\Psi^\dagger = (\langle 1, 1, 1, 1 |, \langle 1, 1, 0, 0 |, \langle 1, 0, 1, 0 |, \langle 0, 1, 0, 1 |, \langle 0, 0, 1, 1 |, \langle 0, 0, 0, 0 |). \quad (8)$$

Theoretical curves for the Fourier transform of $P(\tau)$ are shown in Fig. 4 for various ranges of annealing times. This range controls the frequency resolution $\Delta\Omega$ of the $S(\Omega)$ curves.

B. Disorder in the Transverse Field Calculation

To account for disorder in the Zeeman-like terms, we consider introduce a term $H_\Gamma = \Gamma(s) \sum_n h_n \sigma_n^x$ in the Hamiltonian. In terms of fermions, this term becomes

$$H_\Gamma = \Gamma(s) \sum_n h_n (2\psi_n^\dagger \psi_n - 1). \quad (9)$$

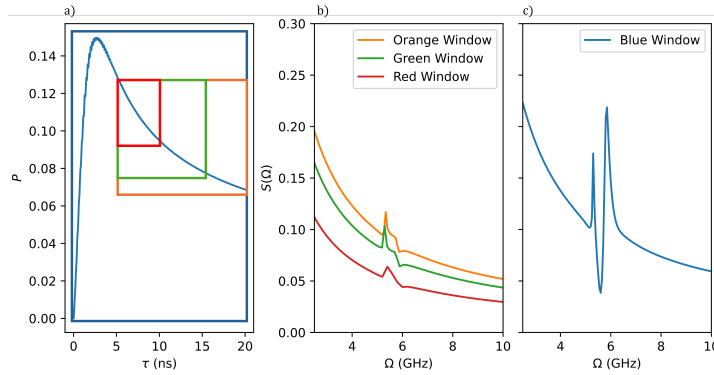


FIG. 4. Sensitivity of $S(\Omega)$ to the range of annealing times included in the Fourier transform. (a) Windows indicate range of annealing times used to calculate the corresponding $S(\Omega)$ curves in (b). The curves in Fig. 2c of the main text were obtained using the (red) window. (c) The double peak structure is most clearly visible for the window $0 \leq \tau \leq 20$ ns.

In k -space, we have

$$H_{\Gamma} = \frac{\Gamma(s)}{\sqrt{N}} \sum_{k,q} h_q \psi_k^{\dagger} \psi_{k-q}, \quad (10)$$

where $h_n = \frac{1}{\sqrt{N}} \sum_k e^{ikn} h_k$. The terms with $q \approx 0$ and $q \approx 2k$ describe elastic scattering and thus dominate for annealing times τ that greatly exceed the characteristic period of the fast oscillations of the system $1/\Omega$. In other words, we ignore the rapidly oscillating terms in the Hamiltonian. What remains is

$$H_{\Gamma} = \frac{\Gamma(s)}{\sqrt{N}} \sum_{0 < k < \pi/2} h_{2k} (\psi_k^{\dagger} \psi_{-k} + \psi_{-k}^{\dagger} \psi_k + \psi_{\pi-k}^{\dagger} \psi_{\pi+k} + \psi_{\pi+k}^{\dagger} \psi_{\pi-k}). \quad (11)$$

These terms now allow the system to access the states $|1, 0, 0, 1\rangle$ and $|0, 1, 1, 0\rangle$ as well. The calculations of $P(\tau)$ for the disordered case thus involve diagonalizing each of the 8×8 blocks.

C. Calibration and shimming for the staggered Ising chain

We follow the iterative shimming methodology of Chern *et al.* [35], adapting it to the symmetry of our one-dimensional staggered Ising chain. The goal is to compensate residual qubit biases and coupler miscalibrations so that, for a given programmed Hamiltonian, the sampled spin configurations respect the expected symmetries of the model.

Symmetry orbits and target observables. The embedded chain has a discrete dihedral symmetry with two natural qubit orbits (even and odd sublattices) and two coupler orbits (strong bonds with target coupling $J_s = J + \Delta J$ and weak bonds with $J_w = J - \Delta J$). In zero longitudinal field ($h_i = 0$) the Ising Hamiltonian is invariant under a global spin flip, so the ensemble-averaged single-qubit magnetization must vanish on each qubit orbit, $\langle \sigma_i^z \rangle_{\mathcal{O}_q} = 0$. For antiferromagnetic couplers we target antialigned spin pairs, i.e., large negative correlations $\langle \sigma_i^z \sigma_j^z \rangle$, with statistics that are uniform within each coupler orbit. We quantify deviations using: (i) the orbit-averaged magnetizations $m_{\mathcal{O}_q} = \langle \sigma_i^z \rangle_{\mathcal{O}_q}$ and (ii) the *frustration probability* for an antiferromagnetic coupler (i, j) ,

$$p_{ij}^{\text{frust}} = \frac{1 + \text{sgn}(J_{ij}) \langle \sigma_i^z \sigma_j^z \rangle}{2}, \quad (12)$$

together with its dispersion within each orbit, $\text{Std}_{\mathcal{O}_c}[p^{\text{frust}}]$.

Gauge averaging and iteration loop. Each iteration consists of: (1) programming a diagnostic instance, (2) collecting $\sim 10^4$ samples over multiple spin-reversal gauges to suppress systematic offsets, (3) computing the orbit-wise observables $\{m_{\mathcal{O}_q}, p_{ij}^{\text{frust}}\}$, and (4) updating local fields and couplers using small corrective “shims.” We employ simple proportional (gradient-descent-like) updates that respect the orbits.

Qubit (flux-bias) shim. We compensate residual single-qubit offsets using the QPU’s per-qubit flux-bias offset controls. Concretely, we apply small corrections $\{\phi_i\}$ through the sampler’s `flux_biases` parameter and update them

orbitwise to drive the ensemble magnetizations toward their symmetry targets:

$$\phi_i \leftarrow \phi_i - \eta_\phi \overline{m}_{\mathcal{O}_q}, \quad i \in \mathcal{O}_q, \quad (13)$$

with a learning rate $\eta_\phi > 0$ and gauge averaging at each iteration. \mathcal{O}_q denotes a qubit orbit, i.e., an equivalence class of qubits related by automorphisms of the embedded Ising graph that preserve the Hamiltonian. Using flux-bias offsets directly targets persistent device-level biases and drift while preserving the programmed problem Hamiltonian; it also aligns with the recommended shimming workflow for Advantage-generation processors [35–37].

Coupler (frustration) shim. To homogenize the effective couplings within each orbit and preserve the intended strong/weak ratio, we apply two complementary adjustments:

$$J_{ij} \leftarrow J_{ij} - \eta_J \delta_{\mathcal{O}_c}(i, j), \quad (i, j) \in \mathcal{O}_c, \quad (14)$$

$$\delta_{\mathcal{O}_c}(i, j) = p_{ij}^{\text{frust}} - \overline{p^{\text{frust}}}_{\mathcal{O}_c} \quad (15)$$

which suppress the intra-orbit dispersion of frustration probabilities. A coupler orbit \mathcal{O}_c consists of all couplers that are symmetry-equivalent under the same automorphism group.

These two steps equalize couplers within orbits and enforce the intended dimerization across orbits. The learning rates η_J are kept small at each annealing time to ensure stable convergence.

Convergence diagnostics. Figure 5(a) shows histograms of the total magnetization over successive iterations: the initially broad, asymmetric distribution collapses toward a narrow, centered peak after shimming. Figure 5(c) displays the evolution of p_{ij}^{frust} across all couplers; the spread within each orbit shrinks iteration by iteration. The corresponding orbit-wise standard deviation $\text{Std}_{\mathcal{O}_c}[p^{\text{frust}}]$, plotted in Figure 5(d), serves as a scalar convergence metric. Once both $|\overline{m}_{\mathcal{O}_q}|$ and $\text{Std}_{\mathcal{O}_c}[p^{\text{frust}}]$ fall below preset thresholds, qubit magnetizations and pair correlations stabilize and the shim is frozen.

Remarks on the staggered chain. Specializing to the dimerized chain helps in two ways. First, the symmetry reduction to two qubit orbits and two coupler orbits yields high measurement statistics per orbit, accelerating convergence. Second, the explicit weak/strong structure provides an internal consistency check, namely after shimming, the hardware-measured ratio of orbit-averaged correlations (or linear response slopes) must match the programmed dimerization to within statistical error. We find that combining qubit-bias and coupler-frustration shims yields a dual calibration of local fields and interactions that is necessary to prevent spurious lifting of degeneracies or distortion of defect sampling in subsequent quench experiments.

Figure 6 shows the embedding of a 160-qubit Ising chain on D-Wave’s Zephyr graph.

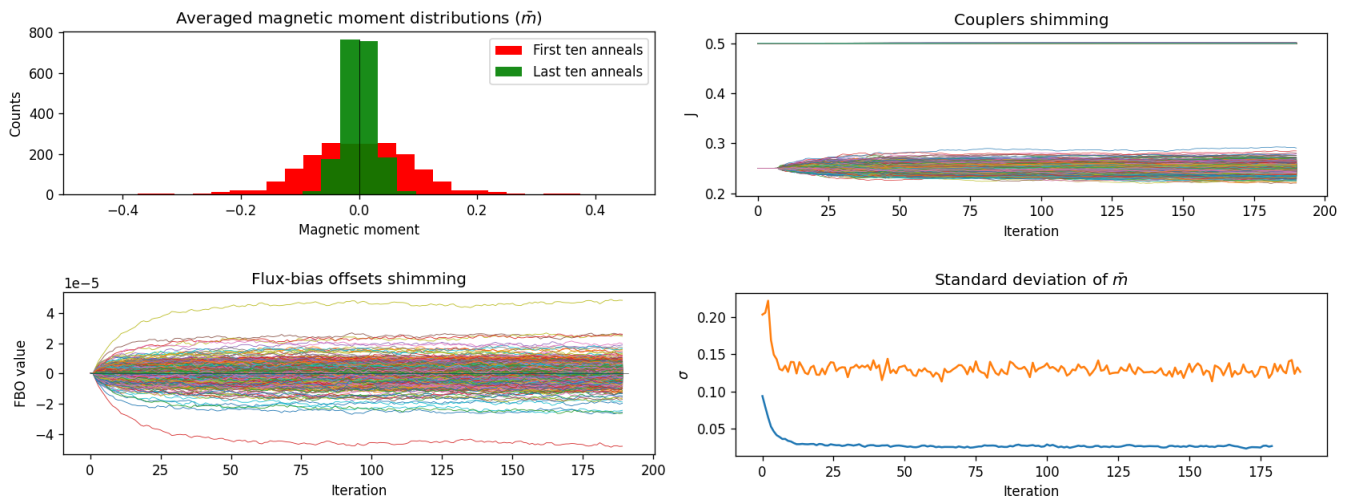


FIG. 5. Results of the iterative shimming procedure applied to the staggered Ising chain for the particular annealing time of $19ns$. a) Histograms of the averaged magnetization \bar{m} for the first ten (red) and last ten (green). The distribution narrows and centers around zero as flux-bias offsets and coupler strengths are refined. b) Evolution of the programmed coupler strengths J_{ij} over successive iterations converging toward stable values. c) Convergence of per-qubit flux-bias offset (FBO) values for gradual suppression of residual local-field biases. d) Standard deviation $\sigma_{\bar{m}}$ of the orbit-averaged magnetization as a function of iteration, indicating rapid stabilization of the ensemble. Together, these panels illustrate how successive flux-bias and coupler adjustments restore symmetry between qubit orbits and minimize frustration, yielding a calibrated embedding faithful to the intended staggered Ising Hamiltonian.

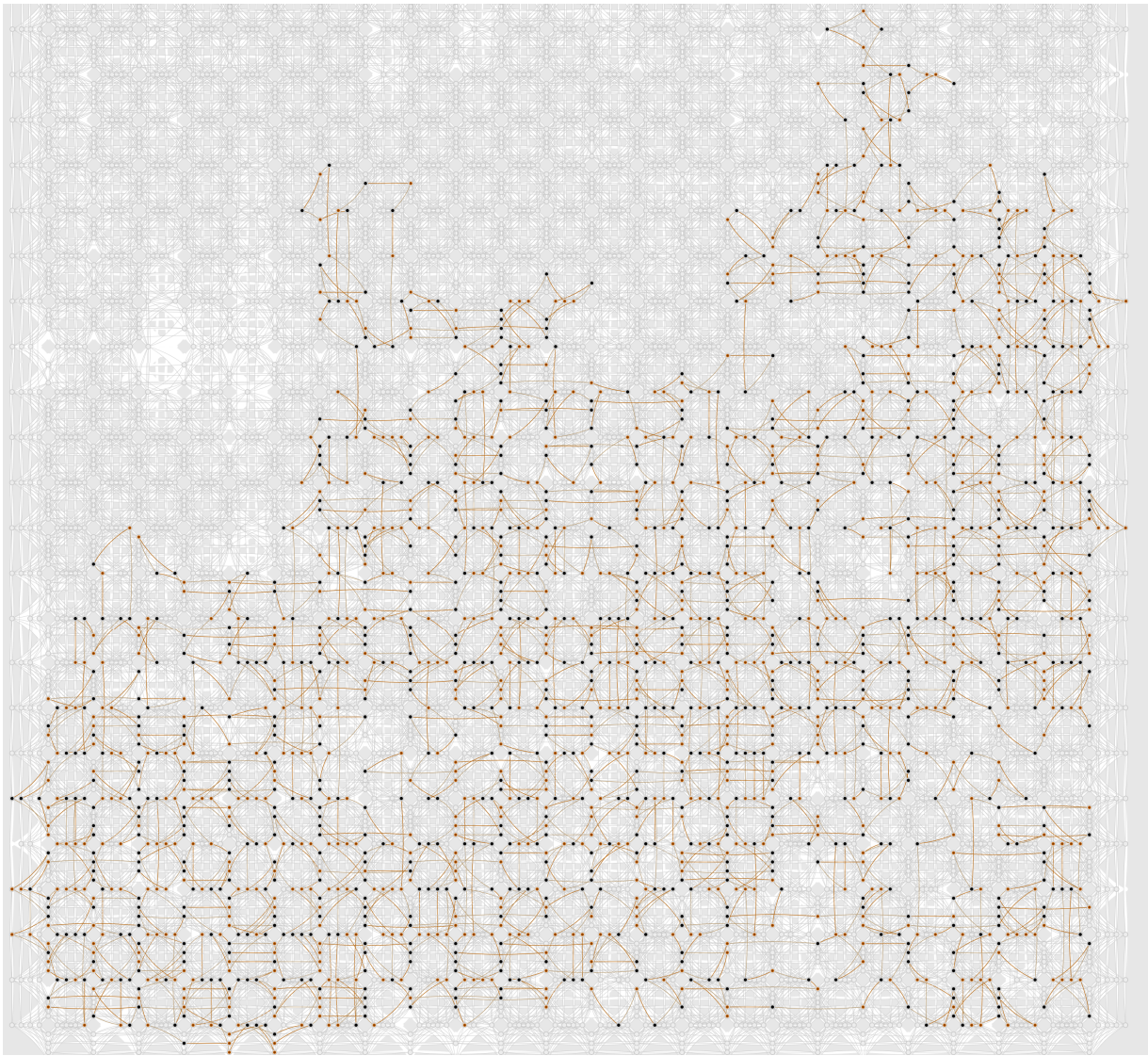


FIG. 6. Visualization of the Zephyr topology of the D-Wave Advantage2 quantum processing unit (QPU) with more than 4,400 qubits. Active qubits (orange and black dots) indicate spin orientations of +1 and -1 in a computed solution. The embedding simultaneously includes four 160-node and four 320-node rings mapped onto the QPU connectivity graph, with couplers represented as orange lines.